RSC Sustainability

ROYAL SOCIETY OF CHEMISTRY

PAPER

View Article Online
View Journal | View Issue

Cite this: *RSC Sustainability*, 2024, **2**, 3507

Atomic layer deposition of Ru nanoclusters on Ba–$LaCeO_x$: a highly efficient catalyst for ammonia synthesis under mild conditions†

Kaiying Wang, ‡[a] Baitang Jin,‡[b] Xiaoqing He[cd] and Xinhua Liang *[ab]

Ammonia synthesis has significant implications for global energy and environmental issues, driving the need for highly active catalysts that operate under mild conditions. This study reports the successful deposition of uniform ~1.0 nm metallic ruthenium (Ru) nanoclusters onto Ba–$LaCeO_x$ particles *via* atomic layer deposition (ALD). The catalytic performance of the ALD-prepared Ru nanoclusters was assessed for ammonia synthesis and compared with two catalysts produced by conventional incipient wetness impregnation. For the ALD-prepared Ru nanoclusters, a pre-reaction H_2-reduction step induced partial encapsulation of suboxide species on Ru sites due to strong metal–support interactions, limiting Ru nanocluster sintering and maintaining a reduced Ru size of 1.7 nm. The electron donation from the reduced support to Ru sites imparted an electron-rich character, which facilitated the weakening of the N≡N bond and promoted the rate-determining step of ammonia synthesis. The ALD-Ru catalysts exhibited competitive ammonia synthesis activity under milder conditions, compared to the impregnated catalysts, with a lower requirement for initial reaction temperature. These results highlight the potential of ALD-synthesized Ru nanoclusters as highly efficient catalysts for low-temperature ammonia production, offering a promising avenue for advancing ammonia synthesis technologies.

Received 4th July 2024
Accepted 5th October 2024

DOI: 10.1039/d4su00350k

rsc.li/rscsus

Sustainability spotlight

Addressing the global need for sustainable energy sources and industrial processes, our research focuses on ammonia synthesis using ruthenium catalysts. This work advances sustainable chemistry by enabling ammonia production under milder conditions, significantly reducing energy consumption and carbon emissions compared to conventional methods. The use of ruthenium catalysts allows for ammonia synthesis at lower temperatures and pressures, enhancing process efficiency and reducing environmental impact. Additionally, the minimal amount of ruthenium required in catalyst promotes resource conservation. This research aligns with UN Sustainable Development Goals 7 (Affordable and Clean Energy), 9 (Industry, Innovation, and Infrastructure), and 13 (Climate Action) by contributing to cleaner industrial processes, innovative catalytic technologies, and climate change mitigation through reduced carbon emissions in ammonia production.

1. Introduction

Ammonia, a cornerstone of the global fertilizer industry, sustains approximately 70% of the world's food production.[1,2] Its role extends beyond agriculture, emerging as a viable energy carrier due to its superior energy density (15.6 MJ L^{-1} for liquid NH_3, 1.7 times that of liquid H_2), carbon neutrality, and logistical advantages in transportation and storage. This positions ammonia as a key player in energy storage solutions, leveraging existing infrastructure for its distribution and handling.[3] The synthesis of ammonia, a process that combines nitrogen and hydrogen, is inherently exothermic and benefits thermodynamically from lower temperatures and higher pressures.[1] Traditionally, the Haber–Bosch process, reliant on iron-based catalysts, has been the standard method for ammonia production.[4] However, this process, operating at temperatures above 450 °C and pressures exceeding 20 MPa, is a significant energy consumer and carbon dioxide emitter, accounting for 2% of global energy usage and 3% of CO_2 emissions.[5]

In response to these challenges, ruthenium-based catalysts have been identified as a promising alternative, offering enhanced activity under less severe conditions: below 400 °C and under 10 MPa. This shift could dramatically reduce both

[a]*Department of Energy, Environmental & Chemical Engineering, Washington University in St. Louis, St. Louis, Missouri, 63130, USA. E-mail: Xinhua.Liang@wustl.edu*

[b]*Linda and Bipin Doshi Department of Chemical and Biochemical Engineering, Missouri University of Science and Technology, Rolla, Missouri 65409, USA*

[c]*Electron Microscopy Core Facility, University of Missouri, Columbia, Missouri 65211, USA*

[d]*Department of Mechanical and Aerospace Engineering, University of Missouri, Columbia, Missouri 65211, USA*

† Electronic supplementary information (ESI) available. See DOI: https://doi.org/10.1039/d4su00350k

‡ Equal contribution to this work.

energy requirements and carbon emissions.[6,7] The development of highly active ruthenium catalysts for ammonia synthesis at these milder conditions has been a focus of recent research. The effectiveness of these catalysts is further improved by the choice of support materials, which can modify the electronic properties of ruthenium, thereby enhancing the overall reaction. Mixed oxide composites have been applied as the support for Ru-based catalysts, such as CeO_2–La_2O_3,[8] CeO_2–MgO,[9] BaO–CeO_2,[10] and La_2O_3–Pr_2O_3.[11] Recent studies have reported that Ru/$LaCeO_x$ and Ru/BaO–$LaCeO_x$ exhibited superior activity in NH_3 synthesis under mild conditions. It has been suggested that further reduction of the support could enhance electron donation from the support,[12–15] enhancing the electron-rich property of Ru and accelerating N_2 activation on Ru sites. During the high-temperature H_2 reduction, the reducible support can be partially reduced by H_2 spillover from the transition metal sites.[16–18]

A key to optimizing ruthenium-based catalysts lies in the precise engineering of the active sites, particularly the B_5-type sites found in ruthenium nanoparticles. These sites, characterized by a cluster of five ruthenium atoms, exhibit a high affinity for nitrogen, facilitating the breaking of the strong N≡N triple bond *via* electron donations to the π-orbitals of N_2 under mild conditions. The optimal performance is observed with hemispherical ruthenium nanoparticles approximately 2 nm in diameter, where the concentration of B_5-type sites is maximized.[19] The method of catalyst preparation plays a crucial role in achieving this configuration. Atomic layer deposition (ALD), a technique that allows for the controlled deposition of metal nanoparticles, emerges as a superior method for preparing ruthenium catalysts.[20,21] By enabling precise control over particle size and the metal–support interface, ALD offers a pathway to highly efficient ammonia synthesis under mild conditions. To the best of our knowledge, this is the first report on utilizing ALD-synthesized Ru catalysts for ammonia synthesis.

Another strategy to enhance ammonia synthesis activity is to perform electronic modification by incorporating a basic promoter into Ru catalysts. The electronic modification approach has significantly improved ammonia synthesis activity.[22–24] The mechanism involves the transfer of electrons from the basic components to the Ru metal. Subsequently, the transfer of electrons from Ru to the antibonding π-orbitals of N_2 weakens the N≡N bond, facilitating N≡N cleavage and promoting ammonia formation. Infrared spectroscopy studies have confirmed the weakening of the N≡N bond by doping with strong basic oxides, with Cs_2O reported as the most effective promoter. Consequently, most highly active Ru catalysts contain Cs_2O as a promoter.[25,26] However, CsOH, which may form in the presence of H_2O impurities in the reactants, has a low melting point (272 °C) and can migrate on the catalyst particle surface or vaporize under reaction conditions, eventually leading to catalyst degradation.[23] On the other hand, BaO has also been reported as an effective promoter, and barium–ruthenium supported on activated carbon (Ba–Ru/AC) catalysts have been employed in commercial industrial processes. Horiuchi *et al.* also reported that ruthenium supported on barium titanate (Ru/$BaTiO_3$) and barium–ruthenium supported on magnesium oxide (Ba–Ru/MgO) exhibited comparable high catalytic activity to cesium–ruthenium supported on magnesium oxide (Cs–Ru/MgO) for ammonia synthesis.[27] These findings suggest that barium is a more favorable promoter compared to cesium for enhancing the ammonia synthesis activity of ruthenium-based catalysts, as it offers superior thermal stability and resistance to deactivation under reaction conditions.

In this work, we employed BaO–$LaCeO_x$ as the catalyst support and utilized the ALD technique to deposit size-controllable Ru nanoclusters on this support for ammonia synthesis under mild conditions. Compared to conventional Ru catalysts prepared by incipient wetness (IW) impregnation using $Ru_3(CO)_{12}$ or $RuCl_3$ precursors, the ALD-prepared Ru/BaO–$LaCeO_x$ catalyst demonstrated competitive activity for ammonia synthesis.

2. Experimental

2.1. Catalyst preparation

The BaO–$LaCeO_x$ support was synthesized by a coprecipitation method for $LaCeO_x$, followed by an impregnation method for Ba addition. An aqueous solution of $La(NO_3)_3 \cdot 6H_2O$ and $Ce(NO_3)_3 \cdot 6H_2O$ was pumped into a concentrated ammonia aqueous solution (28 wt%) to precipitate lanthanum and cerium hydroxides. After filtration and washing with deionized water, the precipitate was added into an aqueous solution of $Ba(OH)_2$, which was stirred for 1 hour. The resulted slurry was evaporated at 80 °C to obtain a powder precursor. This powder was then calcined in air flow at 500 °C, followed by calcination in static air at 700 °C. The final BaO–$LaCeO_x$ support, denoted as BLCO, had a molar composition of Ba : La : Ce = 0.1 : 0.45 : 0.45. Ru nanoclusters were deposited on the BaO–$LaCeO_x$ support by ALD employing a custom-built fluidized bed reactor, as detailed in our previous reports.[28–30] Bis(cyclopentadienyl) ruthenium(II) ($RuCp_2$, Strem, 99%) and O_2 were used as the metal precursor and oxidant, respectively. Prior to ALD, the BaO–$LaCeO_x$ particles were loaded into the ALD reactor and heated overnight at 150 °C under vacuum to remove physisorbed moisture. The ALD process was conducted at 400 °C, with N_2 (Airgas, 99.9%) serving as the carrier gas and purge gas for $RuCp_2$ delivery and reactor purging. Each ALD cycle consisted of the following sequence: $RuCp_2$ precursor dose, N_2 purge, reactor evacuation, O_2 dose, N_2 purge, and reactor evacuation. A total of 30 $RuCp_2$ ALD cycles were performed on the BaO–$LaCeO_x$ support to deposit the Ru nanoclusters, and the catalyst was denoted as Ru/BLCO_ALD. The loading of Ru for the Ru/BLCO_ALD was 0.5 wt% from inductively coupled plasma-optical emission spectroscopy (ICP-OES).

For comparative purposes, ruthenium nanoclusters were also deposited onto the BaO–$LaCeO_x$ support using conventional IW impregnation technique with two different ruthenium precursors with ~0.5 wt% Ru loading. In the first method, ruthenium tris(carbonyl) cluster ($Ru_3(CO)_{12}$) dissolved in tetrahydrofuran (THF) was employed as the precursor. The BaO–$LaCeO_x$ support was impregnated with the $Ru_3(CO)_{12}$/THF

solution under continuous stirring for 12 hours. Subsequently, the solvent was removed *via* rotary evaporation. The impregnated sample was dried overnight in an oven at 80 °C and then calcined at 500 °C for 5 hours in a muffle furnace. This catalyst was denoted as Ru/BLCO_$Ru_3(CO)_{12}$. In the second method, ruthenium trichloride hydrate ($RuCl_3 \cdot xH_2O$) dissolved in deionized water was utilized as the precursor solution for impregnation of the BaO–$LaCeO_x$ support under stirring for 1 hour. The impregnated sample was dried overnight at 80 °C in an oven, followed by calcination at 500 °C for 5 hours in a muffle furnace. This catalyst was labeled as Ru/BLCO_$RuCl_3$.

2.2. Ammonia synthesis reaction

A homemade stainless steel fixed-bed reactor (O.D. = 12.7 mm and I.D. = 9.5 mm) was employed for ammonia synthesis testing. In a typical experiment, ~0.32 g of catalyst was physically mixed with 3.2 g of quartz sand and loaded into the reactor, supported on a quartz wool plug (~50 mg). A K-type thermocouple (Omega Engineering) was positioned in the middle of the reactor to measure the catalyst temperature. High-precision mass flow controllers (Brooks Instruments) regulated the reactant gas flow rates. All inlet gases were passed through a rigorous moisture and oxygen filter system (CRS ZPure LS O_2/H_2O filter) before entering the reactor, effectively eliminating the presence of water vapor and oxygen. The reactor effluent was analyzed by an online gas chromatograph (SRI 8610C) equipped with a 6-foot Hayesep D column for NH_3, CO_2, and H_2O analysis, and a 6-foot molecular sieve 13X column for N_2, H_2, CO, and CH_4 analysis, using a thermal conductivity detector (TCD). Prior to reaction, the catalysts underwent *in situ* reduction at 500 °C for 3 hours under a 20 mL min^{-1} flow of H_2 (UHP grade, Airgas). After reduction, the feed was switched to a reactant mixture of N_2/H_2 (25/75 vol%, UHP grade, Airgas) and the reactor was pressurized to the desired conditions. A back-pressure regulator was used to control the total system pressure, which was monitored by a pressure gauge. The activity was evaluated using the turnover frequency (TOF), which was normalized by both the Ru loading amount and the dispersion of Ru deposited on the supports. The TOF was calculated using the following equation:[31]

$$\mathrm{TOF} = \frac{r_{\mathrm{NH_3}} \times M_{\mathrm{Ru}}}{m_{\mathrm{cat}} \times W \times D}$$

where r_{NH_3} represents the molar production rate of NH_3 (mol s^{-1}) at the reactor outlet, M_{Ru} is the atomic mass of Ru (g mol^{-1}), m_{cat} denotes the weight of the catalyst packed into the reactor (g), D represents the dispersion of Ru deposits. The dispersion (D) was estimated using the equation $D = 12.9/d$,[17] where d is the average Ru particle size (nm) obtained from transmission electron microscopy (TEM) analysis of the reduced samples.

2.3. Catalyst characterizations

The morphology of the fresh and spent catalysts was examined by TEM using an FEI Tecnai F20 instrument. X-ray photoelectron spectroscopy (XPS) was conducted on a Kratos Axis 165 spectrometer to probe the chemical states of the catalysts. Crystalline phases were identified by X-ray diffraction (XRD) using a Philips X'Pert Multi-purpose Diffractometer. The ruthenium loading was quantified by ICP-OES using a PerkinElmer 2000D instrument. Prior to analysis, the samples were digested in aqua regia solution using a 16-position Titan MPS microwave digestion system. Hydrogen temperature-programmed reduction (H_2-TPR) experiments were performed using a Micromeritics AutoChem II 2920 instrument to investigate the reducibility of the catalysts. The samples were pretreated at 300 °C under Ar flow, followed by cooling to room temperature. TPR analysis was then carried out by ramping the temperature from room temperature to 1000 °C with a rate of 10 °C min^{-1} under a 10 vol% H_2/Ar gas mixture. Hydrogen temperature-programmed desorption (H_2-TPD) analysis was conducted using a Micromeritics AutoChem II 2920 instrument to examine the desorption of chemisorbed H_2 from the catalyst surface. The procedure involved exposing the sample to H_2 at 500 °C for 3 hours, followed by a 1 hour hold in H_2 at 50 °C. The catalyst was then purged in 30 mL min^{-1} of Ar for 1 hour before being heated to 600 °C for the final desorption step.

3. Results and discussion

The morphology and structural characteristics of fresh Ru catalysts synthesized *via* different preparation methods were investigated utilizing TEM, as depicted in Fig. 1. In Fig. 1a, the Ru particle size of the fresh Ru/BLCO_ALD catalyst was approximately 1.0 nm. Regarding the fresh Ru/BLCO_$Ru_3(CO)_{12}$ catalyst (Fig. 1b), no discernible particle structure was observed, suggesting that the RuO_2 sites were predominantly present in an amorphous layer structure. Yao *et al.* also reported that an amorphous RuO_2 structure was obtained when utilizing $Ru_3(CO)_{12}$ as the metal precursor.[32] This observation was attributed to the intermolecular forces inherent to $Ru_3(CO)_{12}$ and its strong interaction with the support material. As for the fresh Ru/BLCO_$RuCl_3$ catalyst (Fig. 1c), the size of the Ru nanoclusters was approximately 1.4 nm. Therefore, the morphological and structural characteristics of the fresh Ru catalysts exhibited distinct variations contingent upon the different synthesis methods employed, underscoring the impact of preparation techniques on the resulting catalyst properties.

High-resolution XPS spectra were acquired to investigate the chemical states of C, Ru, O, Ce, Ba, and La in three fresh catalysts prepared by different synthesis methods, as shown in Fig. 2 and S1.† The spectra were deconvoluted and calibrated by fixing the adventitious carbon (C_{adv}) at 284.5 eV. Notably, Ru 3p spectra were also recorded to deconvolute the overlapping C 1s and Ru 3d. For C 1s and Ru 3d spectra in Fig. 2a, the C 1s spectra were deconvoluted into adventitious carbon at 284.5 eV, C–O at 286.4 eV, and C=O at 288.5 eV,[33,34] while Ru 3d spectra were deconvoluted into Ru at 280.2 eV, RuO_2 at 282.0 eV for Ru $3d_{5/2}$, and Ru at 283.9 eV and RuO_2 at 285.2 eV for Ru $3d_{3/2}$. Notably, the Ru nanoclusters prepared by the ALD method consisted of both Ru and RuO_2, whereas the Ru nanoclusters in the IW-prepared catalysts with $Ru_3(CO)_{12}$ or $RuCl_3$ as Ru precursor

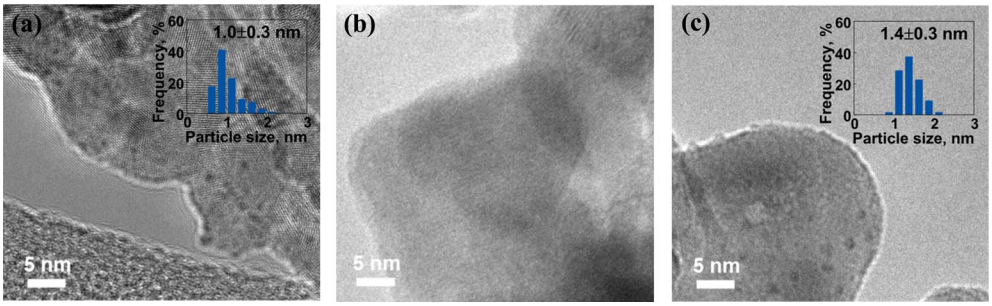

Fig. 1 TEM images of (a) fresh Ru/BLCO_ALD, (b) fresh Ru/BLCO_$Ru_3(CO)_{12}$, and (c) fresh Ru/BLCO_$RuCl_3$.

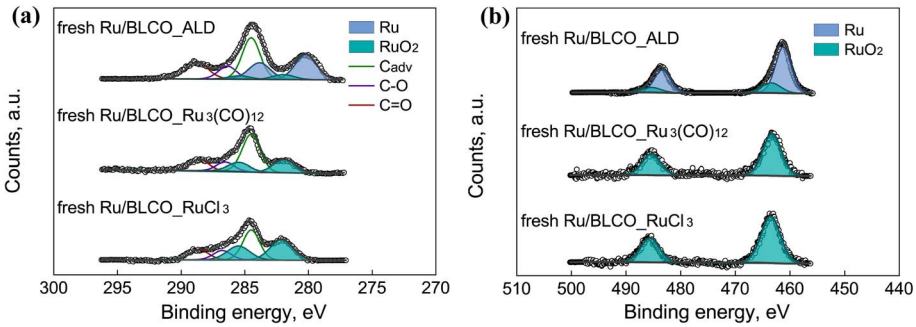

Fig. 2 XPS spectra of (a) C 1s + Ru 3d and (b) Ru 3p of Ru/BLCO_ALD, fresh Ru/BLCO_$Ru_3(CO)_{12}$, and fresh Ru/BLCO_$RuCl_3$.

only consisted of RuO_2. For the Ru 3p spectra in Fig. 2b, the Ru 3p peaks were deconvoluted into Ru at 461.6 eV, RuO_2 at 463.7 eV for Ru $3p_{3/2}$, and Ru at 483.7 eV and RuO_2 at 485.6 eV for Ru $3p_{3/2}$, respectively. Based on the deconvolution results for Ru 3p and Ru 3d, a consistent conclusion was drawn that the Ru nanoclusters prepared by ALD consisted of metallic Ru and oxidized RuO_2, which was different from the catalysts prepared by the traditional IW method. The distinct chemical states of Ru sites originated from the unique ALD growth, and the deposition of metallic Ru by ALD has been reported in numerous studies.[35–38] For the ammonia synthesis reaction, the unique chemical states of the ALD-prepared Ru sites were found to exhibit better interactions with the support in reducing atmosphere, which will be discussed later.

H_2-TPR was performed to investigate the interaction between Ru sites and the BaO–$LaCeO_x$ support for catalysts prepared *via* different preparation methods. As shown in Fig. 3, the BaO–$LaCeO_x$ support revealed two distinct reduction peaks. The first peak, centered at approximately 420 °C, can be attributed to the reduction of surface Ce(IV) species to Ce(III). This lower reduction temperature, compared to pure CeO_2, which typically exhibits its first reduction peak above 490 °C,[39–41] indicates enhanced reducibility of the surface cerium ions. This enhancement can be ascribed to the incorporation of Ba and La into the CeO_2 lattice, which likely introduces oxygen vacancies and modifies the local electronic structure of Ce ions.[42,43] The second reduction peak, observed at around 800 °C, corresponds to the reduction of bulk Ce(IV) to Ce(III). Interestingly, this peak position remained relatively unchanged, compared to pure CeO_2, suggesting that the addition of Ba and La primarily affects the surface properties of the material while leaving the bulk reduction characteristics largely unaltered. During the ammonia synthesis process, where the reduction and reaction temperatures exceeded that required for surface Ce(IV) reduction, the redox behavior of surface Ce cations played a crucial role in influencing the catalyst properties and performance through strong metal–support interactions (SMSI).[44,45] For the supported Ru catalysts, the TPR profiles revealed distinct differences based on the preparation methods. A new reduction peak appeared at ~120 °C for the Ru/BLCO_$Ru_3(CO)_{12}$ and Ru/BLCO_$RuCl_3$ catalysts, which was assigned to the reduction of RuO_2 species.[46–48] The sharp peak at ~120 °C corresponded to free RuO_2, while the broader peak at >150 °C indicated RuO_2

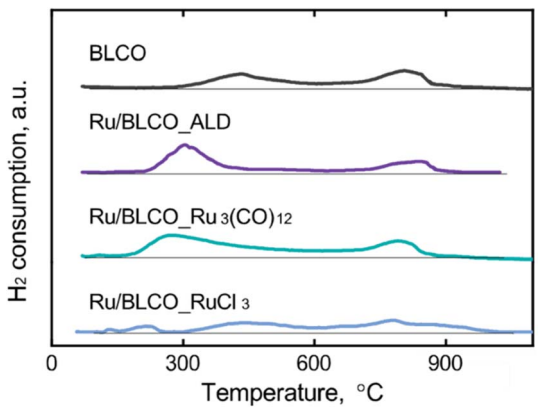

Fig. 3 H_2-TPR profiles BLCO support, Ru/BLCO_ALD, Ru/BLCO_$Ru_3(CO)_{12}$, and Ru/BLCO_$RuCl_3$.

interacting with the BaO–$LaCeO_x$ support. In contrast, no RuO_2 reduction peak was observed for Ru/BLCO_ALD, consistent with the metallic state of Ru in this catalyst. Moreover, the surface Ce(IV) reduction peaks differed among the catalysts. The peak shifted to lower temperatures of ~300 °C for Ru/BLCO_ALD and ~280 °C for Ru/BLCO_$Ru_3(CO)_{12}$, indicating enhanced Ce(IV) reducibility due to the Ru-support interactions. However, for Ru/BLCO_$RuCl_3$, the surface Ce(IV) reduction remained at ~420 °C, suggesting insignificant interaction between Ru and the support. With the assistance of Ru, the CeO_2 was reduced to CeO_x suboxide and thus the mutual interaction between Ru and the reducible oxide support will reconstruct the metal–support interface structure with intimate bonding during the reduction. The improved Ce(IV) reducibility for ALD and $Ru_3(CO)_{12}$-derived catalysts was attributed to hydrogen spillover from Ru sites during reduction, facilitated by smaller Ru particle sizes and SMSI. Consequently, Ce(IV) was reduced to Ce(III), forming a partially reduced CeO_x suboxide that migrated towards Ru nanoclusters and partially encapsulated the Ru nanoclusters due to SMSI. This encapsulated structure enabled electron transfer from the oxygen-deficient CeO_x to Ru sites, enriching the electron density of Ru active sites. Therefore, the different preparation methods resulted in varying degrees of metal–support interactions and Ru particle sizes, which significantly influenced the catalytic properties through modifying the electronic structure of Ru active sites *via* SMSI effects.

To investigate the hydrogen adsorption/desorption characteristics of Ru catalysts and the BLCO support, H_2-TPD experiments were conducted.[49,50] Fig. 4 illustrates the TPD profiles of the samples. The BLCO support exhibited the highest hydrogen desorption temperature among all samples tested. Upon introduction of 0.5 wt% Ru, a notable decrease in desorption temperature was observed. For instance, the Ru/BLCO_ALD catalyst demonstrated a hydrogen desorption temperature of approximately 90 °C, significantly lower than the temperature of 280 °C observed for the bare BLCO support. This indicates that the presence of Ru substantially facilitates hydrogen desorption. Among the Ru-containing catalysts, Ru/BLCO_ALD displayed the lowest desorption temperature, followed by Ru/BLCO_$RuCl_3$ and Ru/BLCO_$Ru_3(CO)_{12}$. This trend suggests that Ru/BLCO_ALD may exhibit superior performance due to its facilitated hydrogen desorption characteristics. Quantitative analysis of hydrogen adsorption capacities revealed that the BLCO support adsorbed 1.9 $cm^3\ g^{-1}$ of hydrogen, while the Ru-containing catalysts showed increased capacities. Ru/BLCO_$RuCl_3$, Ru/BLCO_$Ru_3(CO)_{12}$, and Ru/BLCO_ALD exhibited adsorption capacities of 2.4, 4.0, and 5.7 $cm^3\ g^{-1}$, respectively. The incorporation of Ru significantly enhanced the hydrogen adsorption capacity of the catalysts. This observation aligns with previous research indicating that more reduced ceria can adsorb larger quantities of hydrogen.[9,51] XPS analysis in the following section corroborated these findings. The Ce(III) content was determined to be approximately 27.6% for Ru/BLCO_ALD, compared to 22.0% for the reduced Ru/BLCO_$Ru_3(CO)_{12}$ catalyst and 19.1% for the reduced Ru/BLCO_$RuCl_3$ catalyst. This higher Ce(III) content in Ru/BLCO_ALD is consistent with its enhanced hydrogen adsorption capacity. Therefore, the superior performance of the Ru/BLCO_ALD catalyst can be attributed to its facilitated hydrogen desorption, as evidenced by the lower desorption temperature, and increased hydrogen adsorption capacity, likely due to a higher degree of ceria reduction. These findings underscore the importance of catalyst preparation methods in optimizing hydrogen interaction and, consequently, ammonia synthesis activity.

The morphology and structure of the reduced catalysts were examined using TEM, as shown in Fig. 5 and S2.† After H_2 reduction, the size of Ru sites increased due to the sintering during the high-temperature reduction process. For the ALD-prepared Ru/BLCO_ALD catalyst, the Ru size of the reduced catalyst was at 1.7 nm, compared to 1.0 nm of the as-prepared catalyst. The Ru size of the reduced Ru/BLCO_$Ru_3(CO)_{12}$ catalyst was 2.5 nm, and the Ru size of the reduced Ru/BLCO_$RuCl_3$ catalyst was about 3.2 nm, which were larger than the Ru size of the reduced catalyst prepared by the ALD method. The smaller size for ALD-prepared Ru size indicated that sintering was less significant, which could be ascribed to the SMSI effect. As discussed for the results of XPS and H_2-TPR, the ALD-prepared Ru sites were mainly in the metallic state, whereas the Ru nanoclusters in the other two IW-prepared catalysts were in an oxidized RuO_2 state. The metallic state Ru nanoclusters enhanced SMSI formation during the high-temperature reduction process, which limited the sintering of Ru sites. In addition, the Ru/BLCO_$Ru_3(CO)_{12}$ catalyst seemed to have a stronger SMSI effect than the Ru/BLCO_$RuCl_3$ catalyst, consistent with the H_2-TPR results. Regarding the ammonia synthesis reaction, the size of Ru nanoclusters is a crucial factor, particularly the Ru hemispherical nanoparticles with suitable size at ~2 nm, which are considered optimal for the activation sites such as B5 sites.[19] Besides, some interacting structures were noticed between the metallic Ru nanoparticles and the oxide support, as shown in Fig. S2,† which are different from the fresh catalyst morphology. These structures may result from the reduction process *via* SMSI. In this work, the ALD-prepared Ru/BLCO_ALD catalyst,

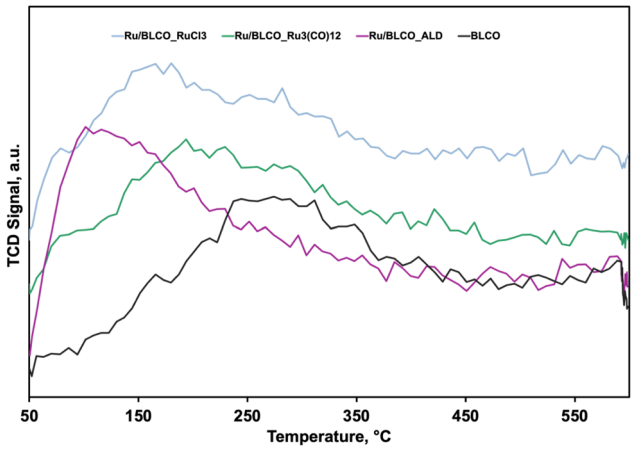

Fig. 4 H_2-TPD profiles BLCO support, Ru/BLCO_ALD, Ru/BLCO_$Ru_3(CO)_{12}$, and Ru/BLCO_$RuCl_3$.

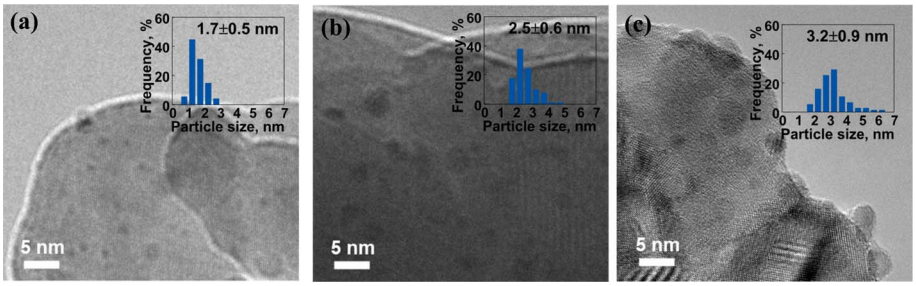

Fig. 5 TEM images of (a) reduced Ru/BLCO_ALD, (b) reduced Ru/BLCO_$Ru_3(CO)_{12}$, and (c) reduced Ru/BLCO_$RuCl_3$ catalyst.

with a suitable Ru size, was expected to exhibit excellent catalytic performance.

High-resolution XPS spectra were conducted to determine the chemical states of C, Ru, O, Ce, Ba, and La after the reduction process for the three catalysts prepared by different methods, as shown in Fig. 6 and S3.† The Ba 3d and La 3d XPS spectra presented in Fig. S3† do not exhibit significant differences among the various catalysts, which can be attributed to several factors. Firstly, Ba and La species are generally less susceptible to reduction by H_2 compared to Ce, potentially resulting in minimal changes in their oxidation states during the reduction process. Secondly, the *ex situ* XPS analysis may limit our ability to detect subtle changes in the chemical states of these elements under reaction conditions. The observed Ba 3d binding energy of approximately 780.2 eV for both fresh and reduced catalysts is consistent with the presence of BaO, as reported in previous studies.[52] However, the exact role and chemical state of Ba in Ru-based ammonia synthesis catalysts remain subjects of ongoing debate in the scientific community. For instance, Truszkiewicz *et al.* proposed that barium undergoes partial reduction during pretreatment, resulting in an active promoter phase composed of a mixture of Ba^0 and BaO. This hypothesis suggests a more complex interplay between the metallic and oxide forms of barium in the catalytic process.[53] Aika *et al.* suggested that barium might exist not only as BaO but also as barium hydroxide. The relative proportions of these two compounds can fluctuate depending on temperature and the partial pressure of water in the inlet stream. Intriguingly, they observed higher ammonia synthesis activities under conditions favoring BaO as the predominant barium-containing phase.[54] But the authors did not exclude the possibility that barium also modified the ruthenium surface, which indicated that barium may be a simultaneous electron and structural promotion.[55] In our specific case, the possibility of $Ba(OH)_2$ formation can be effectively ruled out due to the use of an O_2/H_2O filter in the inlet gas stream. While our *ex situ* XPS

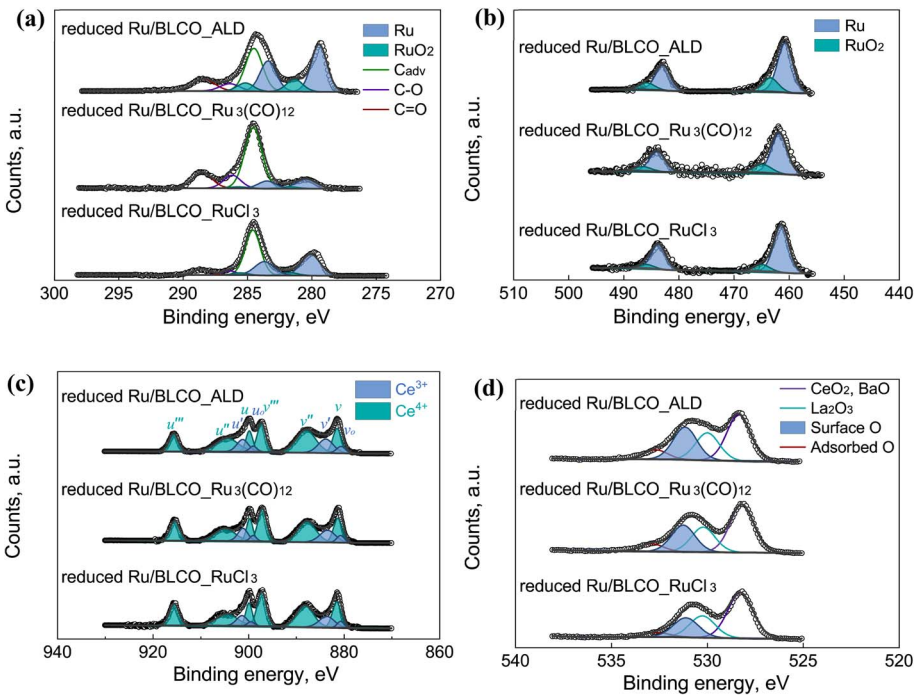

Fig. 6 XPS spectra of (a) C 1s + Ru 3d, (b) Ru 3p, (c) Ce 3d, and (d) O 1s of the reduced Ru/BLCO_ALD, reduced Ru/BLCO_$Ru_3(CO)_{12}$, and reduced Ru/BLCO_$RuCl_3$ catalysts.

analysis did not reveal significant changes in the Ba 3d binding energy after reduction, it's crucial to note that this does not preclude the possibility of barium undergoing partial reduction under H_2 pretreatment conditions. Interestingly, our surface composition analysis, as presented in Table S1,† reveals a notable change in the Ba/Ru surface ratio after H_2 reduction. For the fresh Ru/BLCO_ALD catalyst, we observed a Ba/Ru ratio of 1.66. This ratio increased to 2.24 after reduction, indicating a significant surface enrichment of barium species. This observation aligns with the concept of barium acting as a structural promoter in our catalyst system. Given the complexity of this system and the limitations of *ex situ* characterization techniques, it is evident that the precise mechanism of barium promotion is intimately linked to the state of the promoter under working conditions. To elucidate this mechanism fully, advanced *in situ* and *operando* characterization techniques are required.

Fig. 6a depicts the spectra of C 1s and Ru 3d for the reduced catalysts, and Fig. 6b depicts the spectra of Ru 3p for the reduced catalysts. In Fig. 6a, the C 1s spectra were deconvoluted into adventitious carbon at 284.5 eV, C–O at 286.4 eV, and C=O at 288.5 eV. The adventitious carbon was calibrated at 284.5 eV. Regarding Ru, all the Ru 3p and Ru 3d profiles consisted of both metallic Ru and a small amount of RuO_2. Based on the XPS results of the fresh catalysts and reduced catalysts, RuO_2 in the catalysts was reduced to the metallic Ru during the H_2-reduction process. From the Ru $3d_{5/2}$ region, the peak of the metallic Ru in the reduced Ru/BLCO_ALD was observed at 279.4 eV, which was lower than 280.1 eV for the fresh Ru/BLCO_ALD catalyst, 280.2 eV for the reduced Ru/BLCO_$Ru_3(CO)_{12}$ catalyst, and 280.1 eV for the reduced Ru/BLCO_$RuCl_3$ catalyst. Similar phenomena were observed for the Ru $3p_{3/2}$ region; the metallic Ru peak for Ru/BLCO_ALD was at 460.9 eV, whereas the metallic Ru peak was at 461.4 eV for fresh Ru/BLCO_ALD, 461.5 eV for reduced Ru/BLCO_$Ru_3(CO)_{12}$, and 461.4 eV for reduced Ru/BLCO_$RuCl_3$. The difference confirmed the special shift of Ru chemical states for the Ru/BLCO_ALD catalyst after the H_2-reduction process. The lower binding energy of Ru was ascribed to the electron donation from the support, as reported as the electronic metal–support interaction. Comparing different preparation methods, the metallic Ru sites of the ALD-prepared Ru/BLCO_ALD catalyst might contribute to the construction of electronic metal–support interaction during the reduction process. The electron-rich state of Ru has been reported to enhance the dissociative adsorption of N_2 on Ru sites.[56] The relative concentration of Ru and RuO_2 is listed in Table S2.† Ru% for the fresh Ru/BLCO_ALD catalyst was ~72.3%, whereas the refresh Ru/BLCO_$Ru_3(CO)_{12}$ and Ru/BLCO_$RuCl_3$ catalysts were composed entirely of RuO_2. Ru% for the reduced Ru/BLCO_ALD catalyst was ~77%, which was lower than ~82% for the reduced Ru/BLCO_$Ru_3(CO)_{12}$ catalyst and ~87% for the reduced Ru/BLCO_$RuCl_3$ catalyst. The lower reduction degree of Ru for the reduced Ru/BLCO_ALD catalyst resulted from the partial encapsulation of suboxide due to SMSI during the H_2-reduction process.[57,58]

Based on the Ce 3d and O 1s spectra, the Ce valence and the oxygen species were studied to demonstrate the mutual effect of ALD-deposited Ru on the support. For the Ce 3d spectra in Fig. 6c, the Ce(IV) peaks consisted of Ce $3d_{5/2}$ peaks (v at 881.3 eV, v'' at 887.8 eV, and v''' at 897.2 eV) and Ce $3d_{3/2}$ peaks (u at 899.8 eV, u'' at 904.7 eV, and u''' at 915.6 eV), while Ce(III) consisted of Ce $3d_{5/2}$ peaks (v_o at 880.8 eV and v' at 883.5 eV) and Ce $3d_{3/2}$ peaks (u_o at 899.1 eV and u' at 901.4 eV).[45,59] During the H_2-reduction process, Ce(IV) was partially reduced to Ce(III), forming the CeO_x suboxide. Especially, the H_2 spillover from Ru sites could promote the reduction of Ce(IV) and lead to the encapsulation of CeO_x on Ru nanoclusters, due the SMSI effect. Under this circumstance, the CeO_x interacted mutually with Ru sites, which could influence the catalytic performance. In this work, the reduced Ru/BLCO_ALD catalyst had a higher concentration of Ce(III) than the reduced Ru/BLCO_$Ru_3(CO)_{12}$ and reduced Ru/BLCO_$RuCl_3$ catalysts. The Ce(III) content (calculating from $v_o\%$ + $v'\%$ + $u_o\%$ + $u'\%$) was found to be ~27.6%, as compared to ~22.0% for the reduced Ru/BLCO_$Ru_3(CO)_{12}$ catalyst and ~19.1% for the reduced Ru/BLCO_$RuCl_3$ catalyst. Besides, the independent u''' peak was taken as the diagnostic peak for Ce(IV) content, and the $u'''\%$ was 8.5% for the reduced Ru/BLCO_ALD catalyst, which was lower than 10.2% for the reduced Ru/BLCO_$Ru_3(CO)_{12}$ catalyst and 11.1% for the reduced Ru/BLCO_$RuCl_3$ catalyst. The lower Ce(IV) and higher Ce(III) contents of Ru/BLCO_ALD indicate that the special Ru nanoclusters prepared by ALD provided a stronger H_2 spillover effect, enhancing the reduction of Ce(IV) to Ce(III). As discussed in the previous section, the Ru nanoclusters prepared by ALD were in the metallic state, and the bonding between Ru and BaO–$LaCeO_x$ support was formed during the ALD process. These factors were conducive to enhancing the H_2 spillover effect and achieving a deeper reduction of the oxidized Ce species. This stronger interaction between the metallic Ru and the reduced BaO–$LaCeO_x$ support further enhanced the overall catalytic performance. The atomic composition results are listed in Table S1.† Based on the XPS surface result, higher Ce/Ru trend can be observed after H_2-reduction, which indicates the structure change of Ce species and possible partial decoration of CeO_x on the Ru nanoparticles.

For the O 1s spectra in Fig. 6d, the oxygen species could be fitted into lattice O of La_2O_3 and BaO, lattice O of CeO_2, surface O, and adsorbed O. The lattice O of CeO_2 and BaO was located at ~528.6 eV,[60–62] and the lattice oxygen of La_2O_3 was located at ~530.3 eV.[63] The surface oxygen was located at ~531.2 eV, which consisted of surface low-coordination O, hydroxyl O, and oxygen vacancy sites;[64,65] especially, the oxygen sites in Ce(III)–O were also reported as oxygen vacancy position.[62,66] The adsorbed O was located at ~532.7 eV, mainly originating from adsorbed oxygen-containing molecules (*e.g.*, H_2O and CO_2).[64] Notably, the surface O species for the reduced Ru/BLCO_ALD catalyst reached 28.1%, which is significantly higher than 23.2% for the reduced Ru/BLCO_$Ru_3(CO)_{12}$ catalyst and 21.3% for the reduced Ru/BLCO_$RuCl_3$ catalyst. The increased surface oxygen species was ascribed to the formation of surface oxygen vacancies of the suboxide that was induced by the H_2-reduction process. Studies have demonstrated that the formation of suboxide and oxygen vacancy could enable the electron transfer to the interfacial Ru metallic sties by charge compensation.

During the ammonia synthesis reaction, the excess electron from the suboxide and oxygen vacancies contributed to the weakening of N≡N bond on the Ru nanoclusters, which is the rate determining step of the ammonia synthesis reaction. Therefore, the Ru sites with a negative charge provide higher activity for the dissociation adsorption of N_2 and could achieve higher ammonia synthesis activity.

Fig. 7 depicts the catalytic performance of ammonia synthesis under different conditions (gas hourly space velocity (GHSV) of 3000 and 6000 mL g_{cat}^{-1} h^{-1}, 1.0 and 2.8 MPa) using catalysts prepared by three different methods. At 6000 mL g_{cat}^{-1} h^{-1}, the ammonia synthesis rate increased with the increasing temperature for all the catalysts. However, the ammonia synthesis rate of the Ru/BLCO_ALD catalyst first increased but then decreased at 3000 mL g_{cat}^{-1} h^{-1}, as the reaction rate reached the equilibrium conversion. For instance, the highest ammonia synthesis rate of the Ru/BLCO_ALD catalyst was obtained at 425 °C under 2.8 MPa and 3000 mL g_{cat}^{-1} h^{-1}, with the rate decreasing when the temperature further increased to 450 °C. The ammonia synthesis rates of the Ru/BLCO_$Ru_3(CO)_{12}$ and Ru/BLCO_$RuCl_3$ catalysts increased as the temperature increased within the tested range due to their low activity, which was far from equilibrium. Besides, the ammonia synthesis rates were higher at 6000 mL g_{cat}^{-1} h^{-1} than at 3000 mL g_{cat}^{-1} h^{-1}. For example, at 400 °C and 2.8 MPa, the ammonia synthesis rate for Ru/BLCO_ALD was 9.2 $mmol_{NH_3}$ $gcat^{-1}$ h^{-1} at 6000 mL g_{cat}^{-1} h^{-1}, which was higher than 7.8 $mmol_{NH_3}$ g_{cat}^{-1} h^{-1} at 3000 mL g_{cat}^{-1} h^{-1}. This indicates that the overall catalyst performance at 3000 mL g_{cat}^{-1} h^{-1} might be limited by the low GHSV. Comparing the catalytic performance of different catalysts, the catalytic activity followed the following order: Ru/BLCO_ALD > Ru/BLCO_$Ru_3(CO)_{12}$ > Ru/BLCO_$RuCl_3$ under different conditions, indicating that the Ru nanoclusters prepared by ALD exhibited better activity than the catalysts prepared by the traditional IW method. For instance, at 2.8 MPa and 3000 mL g_{cat}^{-1} h^{-1}, the ammonia synthesis rate for Ru/BLCO_ALD was 7.8 $mmol_{NH_3}$ g_{cat}^{-1} h^{-1}, which was higher than 5.5 $mmol_{NH_3}$ g_{cat}^{-1} h^{-1} for Ru/BLCO_$Ru_3(CO)_{12}$ and 3.8 $mmol_{NH_3}$ g_{cat}^{-1} h^{-1} for Ru/BLCO_$RuCl_3$. For the catalysts prepared by the traditional IW method, Ru/BLCO_$Ru_3(CO)_{12}$ exhibited higher performance than Ru/BLCO_$RuCl_3$, which was consistent with previous report that a Ru-based catalyst prepared using Cl-free Ru precursor was more active than that prepared using Cl-containing Ru precursor, as some of the Cl^- could remain on the Ru surfaces.[25,67]

TOF is a crucial metric that provides insights into the intrinsic activity of catalysts, allowing for a more accurate comparison between different catalytic systems. In this study, we evaluated the TOF values for our prepared catalysts at 6000 mL g_{cat}^{-1} h^{-1}. The obtained TOF values at 350 °C for Ru/BLCO_ALD, Ru/BLCO_$Ru_3(CO)_{12}$, and Ru/BLCO_$RuCl_3$ catalysts are 5.5×10^{-3} s^{-1}, 3.1×10^{-3} s^{-1}, and 1.3×10^{-3} s^{-1}, respectively. These results clearly demonstrate the competitive intrinsic activity of the Ru/BLCO_ALD catalyst, which exhibited a TOF value approximately 1.8 times of Ru/BLCO_$Ru_3(CO)_{12}$ and 4.2 times of Ru/BLCO_$RuCl_3$ under the same reaction conditions. Further investigation revealed a positive correlation between temperature and TOF values for all catalysts, with Ru/BLCO_ALD showing the most pronounced effect. For the Ru/BLCO_ALD catalyst, the TOF increased from 5.5×10^{-3} s^{-1} at 350 °C to 9.1×10^{-3} s^{-1} at 375 °C, representing a 65.5% increase. When the temperature was further raised to 400 °C,

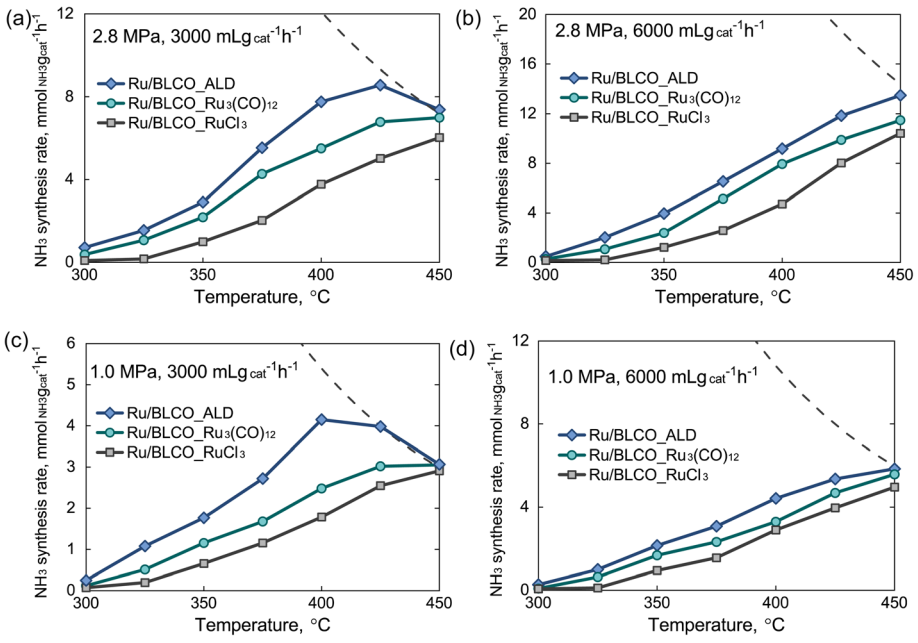

Fig. 7 Catalytic activities of ammonia synthesis using Ru/BLCO_ALD, Ru/BLCO_$Ru_3(CO)_{12}$, and Ru/BLCO_$RuCl_3$ under different conditions: (a) 2.8 MPa and 3000 mL g_{cat}^{-1} h^{-1}, (b) 2.8 MPa and 6000 mL g_{cat}^{-1} h^{-1}, (c) 1.0 MPa and 3000 mL g_{cat}^{-1} h^{-1}, and (d) 1.0 MPa and 6000 mL g_{cat}^{-1} h^{-1}. Note: the dash line shows the equilibrium ammonia synthesis rate.

the TOF reached 1.3×10^{-2} s^{-1}, marking a substantial 136.4% increase from the initial value at 350 °C. Arrhenius plots were constructed for the ammonia synthesis reactions catalyzed by Ru/BLCO_ALD, Ru/BLCO_$Ru_3(CO)_{12}$, and Ru/BLCO_$RuCl_3$ (Fig. S4†). The apparent activation energies (E_a) were calculated to be 60, 68, and 71 kJ mol^{-1} for Ru/BLCO_ALD, Ru/BLCO_$Ru_3(CO)_{12}$, and Ru/BLCO_$RuCl_3$ catalysts, respectively. Notably, the E_a value of Ru/BLCO_ALD (60 kJ mol^{-1}) was significantly lower than that reported for Cs^+/Ru/MgO_500red (100 kJ mol^{-1}).[68] Moreover, it was comparable to the values reported in the literature for other high-performance catalysts, such as 10 wt% Ru/$Ca(NH_2)_2$ (59 kJ mol^{-1})[69] and Ru/$La_{0.5}$-$Ce_{0.5}O_{1.75}$_650red (64 kJ mol^{-1}).[68] The lower apparent activation energy exhibited by Ru/BLCO_ALD suggests a reduced energy barrier for the rate-determining step in the ammonia synthesis reaction. This reduction in E_a is likely another key factor contributing to the high ammonia synthesis rate observed for the Ru/BLCO_ALD catalyst. As described in the previous section, the Ru/BLCO_ALD had a smaller Ru size and electron-rich property arising from the electronic metal–support interaction, compared to the other two catalysts prepared by the IW method. As a result, the Ru nanoclusters by ALD activated the N_2 molecules more effectively and exhibited better catalytic performance in ammonia synthesis.[70]

To comprehensively evaluate the performance of our Ru/BLCO_ALD catalyst, we conducted a thorough comparison with previously reported catalysts from the literature, as presented in Table 1. To ensure a fair and standardized comparison, we normalized the ammonia production rates to per gram of ruthenium, accounting for the varying ruthenium contents employed across different studies. The performance of our Ru/BLCO_ALD catalyst demonstrated competitive activity, compared to many conventional ruthenium nanoparticle catalysts reported in the literature, including Ru/C,[79] Ru/0.3Cs–MgO,[81] and Ba–Ru/γC–Al_2O_3,[75] under comparable reaction conditions. This enhanced performance can be attributed to the unique properties conferred by the ALD technique, such as uniform ruthenium dispersion, SMSI, and optimized electronic properties of the ruthenium species. However, it is important to note that some recently reported ruthenium single-atom catalysts (SACs), such as Ru/HZ SAC[79] and Ru/CeO_2 SAC,[76] exhibited higher catalytic activity than our Ru/BLCO_ALD catalyst. The superior performance of these single-atom catalysts could be primarily attributed to the complete exposure of ruthenium atoms, effectively achieving a theoretical dispersion of 100%. This maximizes the utilization efficiency of the precious metal and provides an abundance of active sites for the reaction. It is crucial to note that the ammonia synthesis mechanism differs significantly between nanoparticle catalysts and SACs. Ruthenium nanoparticles typically follow a direct dissociation mechanism, with B5-type surface sites playing a pivotal role in N_2 activation. In contrast, SACs operate *via* an associative mechanism, which can be more energetically favorable under certain conditions.[79] The remarkable performance of SACs in ammonia synthesis is highly encouraging and opens new avenues for catalyst design using ALD. This technique's precision and versatility make it an ideal method for preparing single atom catalysts.[82–85] Building upon our current findings, our future research will focus on optimizing ALD parameters to synthesize single-atom ruthenium catalysts. This approach aims to combine the benefits of our current system with the advantages of single-atom catalysis. By precisely controlling the ALD process, we anticipate creating a new generation of catalysts that maximize ruthenium atom efficiency and catalytic performance. These next-generation catalysts hold promise for achieving exceptional activity under mild reaction conditions while simultaneously reducing ruthenium usage, thereby addressing both performance and economic considerations in industrial ammonia production.

Table 1 Catalytic performance of Ru-based catalysts on various supports

Samples	T (°C)	P (MPa)	Rate ($mmol_{NH_3}$ g_{Ru}^{-1} h^{-1})	References
Ru/BLCO_ALD	350	1	430	This work
Ru/BLCO_ALD	400	1	830	This work
Ru/BLCO_$Ru_3(CO)_{12}$	400	1	658	This work
Ru/BLCO_$RuCl_3$	400	1	578	This work
Ru/$Ti_{0.18}$–Ce	400	1	767.6	71
Ru/CeO_2-w	400	1	754	72
Ru/LaCe–C	400	1	406	73
Ru–CeO_2-r	400	1	510	74
Ba–Ru/gC–Al_2O_3	400	1	332	75
Ru/CeO_2 SAC	400	1	1058.8	76
Ru/Pr_2O_3	400	0.9	304	23
Ba–Ru SAs/S-1	400	0.1	514.6296	77
Ru/C12A7:e^-	400	0.1	715	78
Ru/HZ SAC	300	1	1260	79
Ru/C	400	1	300	79
Ru/Ba–$Ca(NH_2)_2$	360	0.9	604	22
Ru–Ba/Al_2O_3	400	1	144.34	80
Ru/$Ca(NH_2)_2$	340	0.1	96	69
Ru/0.2Cs–MgO	400	1	717	81

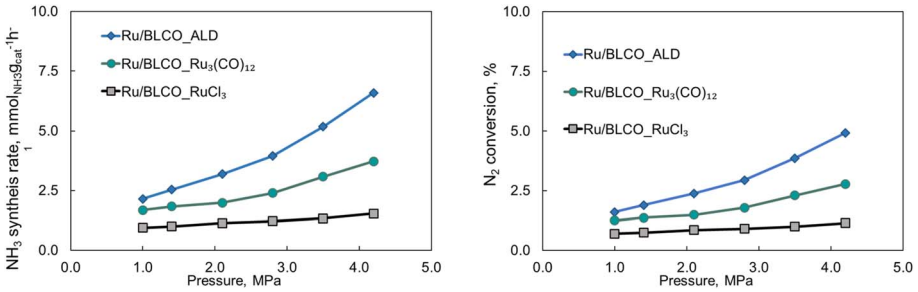

Fig. 8 Effects of pressure on the catalytic activities for ammonia synthesis using Ru/BLCO_ALD, Ru/BLCO_$Ru_3(CO)_{12}$, and Ru/BLCO_$RuCl_3$ at 350 °C and 6000 mL g_{cat}^{-1} h^{-1}.

Fig. 8 illustrates the impact of pressure on the catalytic performance of ammonia synthesis employing different catalysts synthesized *via* three distinct methods at 350 °C and a GHSV of 6000 mL g_{cat}^{-1} h^{-1}. For the Ru/BLCO_$RuCl_3$ catalyst, the ammonia synthesis rate exhibited a slight increase from 0.95 to 1.54 $mmol_{NH_3}$ g_{cat}^{-1} h^{-1} as the pressure rose from 1.0 to 4.2 MPa. The Ru/BLCO_ $Ru_3(CO)_{12}$ catalyst demonstrated a more substantial increase, from 1.68 to 3.72 $mmol_{NH_3}$ g_{cat}^{-1} h^{-1}, over the same pressure range. The Ru/BLCO_ALD catalyst exhibited the most significant enhancement, with the ammonia synthesis rate increasing from 2.15 to 6.6 $mmol_{NH_3}$ g_{cat}^{-1} h^{-1} as the pressure increased from 1.0 to 4.2 MPa. Hydrogen poisoning at elevated hydrogen partial pressures may be a limiting factor for the Ru/BLCO_$RuCl_3$ catalysts in ammonia synthesis.[86,87] In such scenarios, excess hydrogen adatoms can occupy the active sites on the Ru catalyst, inhibiting the efficient dissociative adsorption of N_2 on the Ru surface, thereby suppressing the reactivity of the Ru/BLCO_$RuCl_3$ catalyst for ammonia synthesis. Conversely, for the Ru/BLCO_ALD and Ru/BLCO_$Ru_3(CO)_{12}$ catalysts, the hydrogen spillover effect observed for Ru, as confirmed by H_2-TPR experiments, can mitigate the adsorption of hydrogen on the Ru surface, reducing hydrogen poisoning of the Ru species.[88] Furthermore, it has been reported that the stored hydrogen atoms are reversible and can participate in ammonia synthesis.[78,89] Therefore, the judicious selection of the synthesis method and precursor for Ru catalysts can alleviate their susceptibility to hydrogen poisoning, particularly at elevated partial hydrogen pressures, thereby enhancing their catalytic activity for ammonia synthesis.

The stability of catalysts is a crucial factor for their practical applications in industrial processes. To evaluate the stability under harsh reaction conditions, the best-performing Ru/BLCO_ALD catalyst was subjected to an extended test for ammonia synthesis at 350 °C, 4.2 MPa, and a high GHSV of 6000 mL g^{-1} h^{-1}. As shown in Fig. 9, during the 85 hours test, the Ru/BLCO_ALD catalyst exhibited remarkable stability, maintaining a consistent nitrogen conversion of approximately 5%. Besides, we also conducted another 20 h stability test using the spent catalyst of the 85 h test, and the performance was also stable for the spent catalysts (Fig. S5†). The high stability of the Ru/BLCO_ALD catalyst can be attributed to the SMSI effects, as confirmed by H_2-TPR and XPS analyses. The SMSI phenomenon involves the migration of partially reduced metal oxide species from the support onto the metal nanoparticles, forming a thin oxide overlayer that can enhance the catalyst's stability and activity.[90] Scheme 1 visually represents the SMSI process in ammonia synthesis. The stability of the Ru/BLCO_ALD catalyst under such demanding conditions is noteworthy, as ammonia synthesis typically requires high temperatures and pressures, which can lead to catalyst deactivation over time due to various mechanisms, such as sintering, coking, or poisoning. The stable performance observed in this study suggests that the Ru/BLCO_ALD catalyst is robust and can maintain its catalytic activity for an extended period, even at high temperatures, pressures, and gas flow rates. It is worth noting that the stability test was conducted for 105 hours, which is a significant duration for evaluating catalyst performance under industrial-like conditions. However, further long-term stability studies over

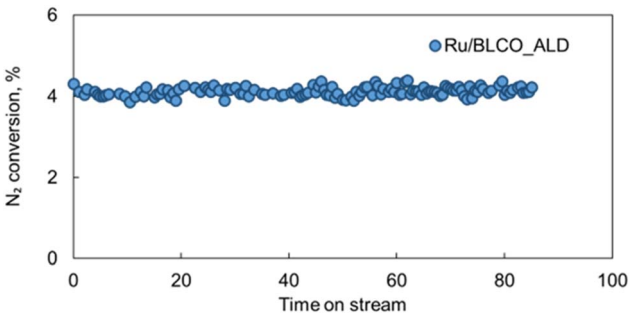

Fig. 9 Stability test of Ru/BLCO_ALD for ammonia synthesis under conditions of 350 °C, 4.2 MPa, and 6000 mL g_{cat}^{-1} h^{-1} for a total of 85 hours.

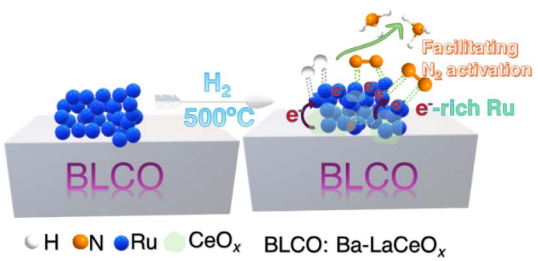

Scheme 1 The SMSI enhanced ammonia synthesis process.

hundreds or thousands of hours is necessary to fully assess the catalyst's lifetime and potential for commercial applications.

4. Conclusion

In this work, Ru/Ba–$LaCeO_x$ (Ru/BLCO) catalysts for ammonia synthesis were synthesized *via* three distinct methods: ALD utilizing $RuCp_2$ as the precursor, and IW employing $Ru_3(CO)_{12}$ and $RuCl_3$ as ruthenium precursors. The ALD technique yielded highly dispersed metallic Ru nanoclusters with a uniform size of 1.0 nm, whereas the IW method resulted in larger Ru nanoclusters predominantly in the RuO_2 phase. For the ALD-prepared Ru/BLCO catalyst, SMSI effects were induced during the hydrogen reduction process, leading to partial encapsulation of the Ru nanoclusters by a suboxide layer. This encapsulation mitigated detrimental sintering of the Ru nanoclusters and facilitated electron donation from the reduced support to the Ru sites, enabling the formation of an electronic metal–support interaction between Ru and the reduced support. The electronic metal–support interaction increased the negative charge density on the Ru sites. The excess electrons on the Ru sites weakened the N≡N bond, thereby enhancing the rate-determining step for ammonia synthesis. Consequently, the ALD-prepared Ru/BLCO catalysts exhibited competitive catalytic activity for ammonia synthesis under milder conditions and lower initial temperature requirements compared to the IW-prepared catalysts, demonstrating promising potential for practical applications in ammonia synthesis catalysts.

Data availability

The data will be made available on request.

Conflicts of interest

There are no conflicts to declare.

Acknowledgements

This work was supported in part by the U.S. National Science Foundation (Award Number 2306177) and Linda and Bipin Doshi endowment of Missouri University of Science and Technology.

References

1 V. S. Marakatti and E. M. Gaigneaux, *ChemCatChem*, 2020, **12**, 5838–5857.
2 A. Mani, T. Budd and E. Maine, *RSC Sustainability*, 2024, **2**, 903–927.
3 A. Valera-Medina, H. Xiao, M. Owen-Jones, W. I. David and P. Bowen, *Prog. Energy Combust. Sci.*, 2018, **69**, 63–102.
4 N. Salmon and R. Bañares-Alcántara, *RSC Sustainability*, 2023, **1**, 923–937.
5 S. A. Matlin, G. Mehta, S. E. Cornell, A. Krief and H. Hopf, *RSC Sustainability*, 2023, **1**, 1704–1721.
6 N. Saadatjou, A. Jafari and S. Sahebdelfar, *Chem. Eng. Commun.*, 2015, **202**, 420–448.
7 Q. Wang, J. Guo and P. Chen, *J. Energy Chem.*, 2019, **36**, 25–36.
8 X. Luo, R. Wang, J. Ni, J. Lin, B. Lin, X. Xu and K. Wei, *Catal. Lett.*, 2009, **133**, 382–387.
9 X. Wang, J. Ni, B. Lin, R. Wang, J. Lin and K. Wei, *Catal. Commun.*, 2010, **12**, 251–254.
10 X.-L. Yang, W.-Q. Zhang, C.-G. Xia, X.-M. Xiong, X.-Y. Mu and B. Hu, *Catal. Commun.*, 2010, **11**, 867–870.
11 Y. Ogura, K. Tsujimaru, K. Sato, S.-I. Miyahara, T. Toriyama, T. Yamamoto, S. Matsumura and K. Nagaoka, *ACS Sustain. Chem. Eng.*, 2018, **6**, 17258–17266.
12 Y. Ogura, K. Sato, S.-I. Miyahara, Y. Kawano, T. Toriyama, T. Yamamoto, S. Matsumura, S. Hosokawa and K. Nagaoka, *Chem. Sci.*, 2018, **9**, 2230–2237.
13 Y. Ogura, T. Asai, K. Sato, S.-I. Miyahara, T. Toriyama, T. Yamamoto, S. Matsumura and K. Nagaoka, *Energy Technol.*, 2020, **8**, 2000264.
14 K. Sato, S.-i. Miyahara, Y. Ogura, K. Tsujimaru, Y. Wada, T. Toriyama, T. Yamamoto, S. Matsumura and K. Nagaoka, *ACS Sustain. Chem. Eng.*, 2020, **8**, 2726–2734.
15 W. Han, Z. Li and H. Liu, *J. Rare Earths*, 2019, **37**, 492–499.
16 X. Fan, K. Wang, X. He, S. Li, M. Yu and X. Liang, *Carbon Resour. Convers.*, 2024, **7**, 100184.
17 Y. Guo, S. Mei, K. Yuan, D.-J. Wang, H.-C. Liu, C.-H. Yan and Y.-W. Zhang, *ACS Catal.*, 2018, **8**, 6203–6215.
18 C. Li, M. Li, Y. Zheng, B. Fang, J. Lin, J. Ni, B. Lin and L. Jiang, *Appl. Catal., B*, 2023, **320**, 100184.
19 C. J. H. Jacobsen, S. Dahl, P. L. Hansen, E. Törnqvist, L. Jensen, H. Topsøe, D. V. Prip, P. B. Møenshaug and I. Chorkendorff, *J. Mol. Catal. A: Chem.*, 2000, **163**, 19–26.
20 B. Zhang and Y. Qin, *ACS Catal.*, 2018, **8**, 10064–10081.
21 L. Cao and J. Lu, *Catal. Sci. Technol.*, 2020, **10**, 2695–2710.
22 M. Kitano, Y. Inoue, M. Sasase, K. Kishida, Y. Kobayashi, K. Nishiyama, T. Tada, S. Kawamura, T. Yokoyama, M. Hara and H. Hosono, *Angew. Chem.*, 2018, **57**, 2648–2652.
23 K. Sato, K. Imamura, Y. Kawano, S. I. Miyahara, T. Yamamoto, S. Matsumura and K. Nagaoka, *Chem. Sci.*, 2017, **8**, 674–679.
24 W. Li, S. Wang and J. Li, *Chem.–Asian J.*, 2019, **14**, 2815–2821.
25 S.-Y. Chen, C.-L. Chang, M. Nishi, W.-C. Hsiao, Y. I. A. Reyes, H. Tateno, H.-H. Chou, C.-M. Yang, H.-Y. T. Chen, T. Mochizuki, H. Takagi and T. Nanba, *Appl. Catal., B*, 2022, **310**, 121269.
26 W. Rarogpilecka, E. Miskiewicz, S. Jodzis, J. Petryk, D. Lomot, Z. Kaszkur, Z. Karpinski and Z. Kowalczyk, *J. Catal.*, 2006, **239**, 313–325.
27 Y. Horiuchi, G. Kamei, M. Saito and M. Matsuoka, *Chem. Lett.*, 2013, **42**, 1282–1284.
28 Z. Shang, S. Li, L. Li, G. Liu and X. Liang, *Appl. Catal., B*, 2017, **201**, 302–309.
29 B. Jin, K. Wang, H. Yu, X. He and X. Liang, *Chem. Eng. J.*, 2023, **459**, 141611.
30 K. Wang, X. He, J. C. Wang and X. Liang, *Nanotechnology*, 2022, **33**, 215602.

31 H. Kim, A. Jan, D. H. Kwon, H. I. Ji, K. J. Yoon, J. H. Lee, Y. Jun, J. W. Son and S. Yang, *Small*, 2023, **19**, e2205424.
32 D. Liu, T. Ding, L. Wang, H. Zhang, L. Xu, B. Pang, X. Liu, H. Wang, J. Wang, K. Wu and T. Yao, *Nat. Commun.*, 2023, **14**, 1720.
33 B. Jin, Z. Shang, S. Li, Y.-B. Jiang, X. Gu and X. Liang, *Catal. Sci. Technol.*, 2020, **10**, 3212–3222.
34 B. Jin, S. Li and X. Liang, *Fuel*, 2021, **284**, 119082.
35 S.-J. Park, W.-H. Kim, W. Maeng and H. Kim, *Microelectron. Eng.*, 2008, **85**, 39–44.
36 X. Jiang, T. M. Gür, F. B. Prinz and S. F. Bent, *Chem. Mater.*, 2010, **22**, 3024–3032.
37 E. Färm, S. Lindroos, M. Ritala and M. Leskelä, *Chem. Mater.*, 2012, **24**, 275–278.
38 J. Hämäläinen, M. Ritala and M. Leskelä, *Chem. Mater.*, 2014, **26**, 786–801.
39 Z. Ni, X. Djitcheu, X. Gao, J. Wang, H. Liu and Q. Zhang, *Sci. Rep.*, 2022, **12**, 5344.
40 A. Jan, J. Shin, J. Ahn, S. Yang, K. J. Yoon, J. W. Son, H. Kim, J. H. Lee and H. I. Ji, *RSC Adv.*, 2019, **9**, 27002–27012.
41 Z. Ma, S. Zhao, X. Pei, X. Xiong and B. Hu, *Catal. Sci. Technol.*, 2017, **7**, 191–199.
42 K. Singh, R. Kumar and A. Chowdhury, *Mater. Today: Proc.*, 2018, **5**, 22993–22997.
43 B. M. Reddy, L. Katta and G. Thrimurthulu, *Chem. Mater.*, 2009, **22**, 467–475.
44 B. Fang, F. Liu, C. Zhang, C. Li, J. Ni, X. Wang, J. Lin, B. Lin and L. Jiang, *ACS Sustain. Chem. Eng.*, 2021, **9**, 8962–8969.
45 B. Lin, B. Fang, Y. Wu, C. Li, J. Ni, X. Wang, J. Lin, C.-t. Au and L. Jiang, *ACS Catal.*, 2021, **11**, 1331–1339.
46 J. Zhou, Z. Gao, G. Xiang, T. Zhai, Z. Liu, W. Zhao, X. Liang and L. Wang, *Nat. Commun.*, 2022, **13**, 327.
47 K. Shun, K. Mori, S. Masuda, N. Hashimoto, Y. Hinuma, H. Kobayashi and H. Yamashita, *Chem. Sci.*, 2022, **13**, 8137–8147.
48 D. Fu, X. Wu, B. Cui, Y. Guo, H. Wang, J. Han, Q. Ge and X. Zhu, *ChemCatChem*, 2021, **13**, 4814–4823.
49 Y. Baik, M. Kwen, K. Lee, S. Chi, S. Lee, K. Cho, H. Kim and M. Choi, *J. Am. Chem. Soc.*, 2023, **145**, 11364–11374.
50 B. Lin, Y. Liu, L. Heng, X. Wang, J. Ni, J. Lin and L. Jiang, *Ind. Eng. Chem. Res.*, 2018, **57**, 9127–9135.
51 L. Zhang, J. Lin, J. Ni, R. Wang and K. Wei, *Catal. Commun.*, 2011, **15**, 23–26.
52 M. Hattori, T. Mori, T. Arai, Y. Inoue, M. Sasase, T. Tada, M. Kitano, T. Yokoyama, M. Hara and H. Hosono, *ACS Catal.*, 2018, **8**, 10977–10984.
53 E. Truszkiewicz, W. Raróg-Pilecka, K. Schmidt-Szałowski, S. Jodzis, E. Wilczkowska, D. Łomot, Z. Kaszkur, Z. Karpiński and Z. Kowalczyk, *J. Catal.*, 2009, **265**, 181–190.
54 H. S. Zeng, K. Inazu and K.-I. Aika, *J. Catal.*, 2002, **211**, 33–41.
55 A. Cao, V. J. Bukas, V. Shadravan, Z. Wang, H. Li, J. Kibsgaard, I. Chorkendorff and J. K. Norskov, *Nat. Commun.*, 2022, **13**, 2382.
56 N. Kuganathan, H. Hosono, A. L. Shluger and P. V. Sushko, *J. Am. Chem. Soc.*, 2014, **136**, 2216–2219.
57 X. Wang, X. Yang, G. Pei, J. Yang, J. Liu, F. Zhao, F. Jin, W. Jiang, H. Ben and L. Zhang, *Carbon Energy*, 2023, **6**, e391.
58 B. M. Stühmeier, R. J. Schuster, L. Hartmann, S. Selve, H. A. El-Sayed and H. A. Gasteiger, *J. Electrochem. Soc.*, 2022, **169**, 034519.
59 B. Jin, S. Li and X. Liang, *Ind. Eng. Chem. Res.*, 2021, 10377–10386.
60 O. Karslıoğlu, L. Trotochaud, I. Zegkinoglou and H. Bluhm, *J. Electron Spectrosc. Relat. Phenom.*, 2018, **225**, 55–61.
61 G. Zhou, H. Liu, K. Cui, A. Jia, G. Hu, Z. Jiao, Y. Liu and X. Zhang, *Appl. Surf. Sci.*, 2016, **383**, 248–252.
62 F. Meng, Z. Fan, C. Zhang, Y. Hu, T. Guan and A. Li, *J. Mater. Sci.*, 2017, **33**, 444–451.
63 P. Fleming, R. A. Farrell, J. D. Holmes and M. A. Morris, *J. Am. Ceram. Soc.*, 2010, **93**, 1187–1194.
64 S. Chen, L. Zeng, H. Tian, X. Li and J. Gong, *ACS Catal.*, 2017, **7**, 3548–3559.
65 K. Wang, X. He and X. Liang, *Int. J. Hydrogen Energy*, 2024, **66**, 195–207.
66 K. Wang, S. Li, M. Yu and X. Liang, *Energies*, 2024, **17**, 839.
67 A. Miyazaki, I. Balint, K.-I. Aika and Y. Nakano, *J. Catal.*, 2001, **204**, 364–371.
68 Y. Ogura, K. Sato, S. I. Miyahara, Y. Kawano, T. Toriyama, T. Yamamoto, S. Matsumura, S. Hosokawa and K. Nagaoka, *Chem. Sci.*, 2018, **9**, 2230–2237.
69 Y. Inoue, M. Kitano, K. Kishida, H. Abe, Y. Niwa, M. Sasase, Y. Fujita, H. Ishikawa, T. Yokoyama, M. Hara and H. Hosono, *ACS Catal.*, 2016, **6**, 7577–7584.
70 C. Li, Y. Shi, Z. Zhang, J. Ni, X. Wang, J. Lin, B. Lin and L. Jiang, *J. Energy Chem.*, 2021, **60**, 403–409.
71 C. Li, Z. Zhang, Y. Zheng, B. Fang, J. Ni, J. Lin, B. Lin, X. Wang and L. Jiang, *Chem. Eng. Sci.*, 2022, **251**, 117434.
72 C. Li, M. Li, Y. Zheng, B. Fang, J. Lin, J. Ni, B. Lin and L. Jiang, *Appl. Catal., B*, 2023, **320**, 121982.
73 C. Li, Y. Zheng, M. Li, B. Fang, J. Lin, J. Ni, X. Wang, B. Lin and L. Jiang, *Int. J. Hydrogen Energy*, 2022, **47**, 23240–23248.
74 B. Lin, Y. Liu, L. Heng, X. Wang, J. Ni, J. Lin and L. Jiang, *Ind. Eng. Chem. Res.*, 2018, **57**, 9127–9135.
75 B. Lin, L. Heng, H. Yin, B. Fang, J. Ni, X. Wang, J. Lin and L. Jiang, *Ind. Eng. Chem. Res.*, 2019, **58**, 10285–10295.
76 B. Lin, Y. Wu, B. Fang, C. Li, J. Ni, X. Wang, J. Lin and L. Jiang, *Chin. J. Catal.*, 2021, **42**, 1712–1723.
77 J.-Z. Qiu, J. Hu, J. Lan, L.-F. Wang, G. Fu, R. Xiao, B. Ge and J. Jiang, *Chem. Mater.*, 2019, **31**, 9413–9421.
78 M. Kitano, Y. Inoue, Y. Yamazaki, F. Hayashi, S. Kanbara, S. Matsuishi, T. Yokoyama, S. W. Kim, M. Hara and H. Hosono, *Nat. Chem.*, 2012, **4**, 934–940.
79 X. Wang, L. Li, Z. Fang, Y. Zhang, J. Ni, B. Lin, L. Zheng, C.-t. Au and L. Jiang, *ACS Catal.*, 2020, **10**, 9504–9514.
80 B. Lin, L. Heng, B. Fang, H. Yin, J. Ni, X. Wang, J. Lin and L. Jiang, *ACS Catal.*, 2019, **9**, 1635–1644.
81 L. Liu, X. Zhang, X. Ju, J. Feng, J. Wang and P. Chen, *Dalton Trans.*, 2021, **50**, 12074–12078.
82 X. Wang, B. Jin, Y. Jin, T. Wu, L. Ma and X. Liang, *ACS Appl. Nano Mater.*, 2020, **3**, 2867–2874.
83 J. Fonseca and J. Lu, *ACS Catal.*, 2021, **11**, 7018–7059.
84 K. Wang, X. Wang and X. Liang, *ChemCatChem*, 2020, **13**, 28–58.

85 L. Zhang, M. N. Banis and X. Sun, *Natl. Sci. Rev.*, 2018, **5**, 628–630.
86 B. Lin, Y. Wu, B. Fang, C. Li, J. Ni, X. Wang, J. Lin and L. Jiang, *Chin. J. Catal.*, 2021, **42**, 1712–1723.
87 S. Wu, Y.-K. Peng, T.-Y. Chen, J. Mo, A. Large, I. McPherson, H.-L. Chou, I. Wilkinson, F. Venturini, D. Grinter, P. Ferrer Escorihuela, G. Held and S. C. E. Tsang, *ACS Catal.*, 2020, **10**, 5614–5622.
88 J. Huang, M. Yuan, X. Li, Y. Wang, M. Li, J. Li and Z. You, *J. Catal.*, 2020, **389**, 556–565.
89 Y. Kobayashi, Y. Tang, T. Kageyama, H. Yamashita, N. Masuda, S. Hosokawa and H. Kageyama, *J. Am. Chem. Soc.*, 2017, **139**, 18240–18246.
90 C. Li, F. Liu, Y. Shi, Y. Zheng, B. Fang, J. Lin, J. Ni, X. Wang, B. Lin and L. Jiang, *ACS Sustain. Chem. Eng.*, 2021, **9**, 4885–4893.